



Applied Computational
Electromagnetics Society



Newsletter
Volume 18 – No. 3
ISSN 1056-9170



November 2003



**APPLIED COMPUTATIONAL ELECTROMAGNETICS SOCIETY
(ACES)**

NEWSLETTER

Vol. 18 No. 3

November 2003

TABLE OF CONTENTS

COMMITTEE REPORTS

Election/Nomination Committee – Rene Allard
ACES Board of Directors Election Results5

CEM News from Europe – Pat Foster6

DEPARTMENTS

Practical CEMist
“The J-Pole Antenna”
R.P. Haviland 8

TUTORIAL ARTICLE – “Implementing the Locally-Corrected Nystrom Method”

Stephen D. Gedney 15

ANNOUNCEMENTS:

The 20th Annual Review of Progress in Applied Computational Electromagnetics
Call for Papers 28

APPLICATION for ACES Membership, Newsletter and Journal Subscription..... 30

ADVERTISING Rates..... 31

DEADLINE for Submission of Articles 31

Last Word31

PERMANENT STANDING COMMITTEES OF ACES, INC.
--

COMMITTEE	CHAIRMAN	ADDRESS
NOMINATION & ELECTIONS	Rene Allard	Penn State University PO Box 30 State College, PA 16804-0030 rja5@psu.edu
FINANCE	Andrew Peterson	Georgia Institute of Technology School of ECE Atlanta, GA 30332-0250 peterson@ece.gatech.edu
PUBLICATIONS	Atef Elsherbeni	EE Department, Anderson Hall University of Mississippi University, MS 38677 atef@olemiss.edu
CONFERENCE	Osama Mohammed	Florida International University ECE Department Miami, FL 33174 mohammed@fiu.edu
AWARDS	Ray Perez	Martin Marietta Astronautics MS 58700, PO Box 179 Denver, CO 80201 ray.j.perez@lmco.com

MEMBERSHIP ACTIVITY COMMITTEES OF ACES, INC.

COMMITTEE	ADDRESS	CHAIRMAN
SOFTWARE VALIDATION	Bruce Archambeault	IBM 3039 Cornwallis Road, PO Box 12195; Dept. 18DA B306 Research Triangle Park, NC 27709 barch@us.ibm.com
HISTORICAL	Robert Bevensee	BOMA Enterprises PO Box 812 Alamo, CA 94507-0812 rmbevensee@cs.com
CONSTITUTION & BYLAWS	Leo Kempel	2120 Engineering Building Michigan State University East Lansing, MI 48824 kempel@egr.msu.edu
MEMBERSHIP & COMMUNICATIONS	Vicente Rodriguez	ETS-LINDGREN L.P. 1301 Arrow Point Drive Cedar Park, TX 78613 rodriguez@ieee.org
INDUSTRIAL RELATIONS	Andy Drodz	ANDRO Consulting Services PO Box 543 Rome, NY 13442-0543 androl@aol.com

ACES NEWSLETTER STAFF

EDITOR-IN-CHIEF, NEWSLETTER

Bruce Archambeault
IBM
3039 Cornwallis Road, PO Box 12195
Dept. 18DA B306
Research Triangle Park, NC 27709
Phone: 919-486-0120
email: barch@us.ibm.com

EDITOR-IN-CHIEF, PUBLICATIONS

Atef Elsherbeni
EE Department, Anderson Hall
University of Mississippi
University, MS 38677
Email: atef@olemiss.edu

ASSOCIATE EDITOR-IN-CHIEF

Ray Perez
Martin Marietta Astronautics
MS 58700, PO Box 179
Denver, CO 80201
Phone: 303-977-5845
Fax: 303-971-4306
email: ray.j.perez@lmco.com

MANAGING EDITOR

Richard W. Adler
Naval Postgraduate School/ECE Dept.
Code ECAB, 833 Dyer Road,
Monterey, CA 93943-5121
Phone: 831-646-1111
Fax: 831-649-0300
email: rwa@attglobal.net

EDITORS

CEM NEWS FROM EUROPE

Pat R. Foster
Microwaves and Antenna Systems
16 Peachfield Road
Great Malvern, Worc. UK WR14 4AP
Phone: +44 1684 5744057
Fax: +44 1684 573509
email: prf@maasdesign.co.uk

TECHNICAL FEATURE ARTICLE

Andy Drozd
ANDRO Consulting Services
PO Box 543
Rome, NY 13442-0543
Phone: 315-337-4396
Fax: 314-337-4396
email: androl@aol.com

THE PRACTICAL CEMIST

W. Perry Wheless, Jr.
University of Alabama
PO Box 11134
Tuscaloosa, AL 35486-3008
Phone: 205-348-1757
Fax: 205-348-6959
Email: wwheless@ualvm.ua.edu

MODELER'S NOTES

Gerald Burke
Lawrence Livermore National Labs.
Box 5504/L-156
Livermore, CA 94550
Phone: 510-422-8414
Fax: 510-422-3013
email: burke2@llnl.gov

PERSPECTIVES IN CEM

Manos M. Tentzeris
Georgia Institute of Technology
ECE Dept.
Atlanta, GA 30332-0250
Phone: 404-385-0378
email: cენტze@ece.gatech.edu

TUTORIAL

J. Alan Roden
IBM Microelectronics
Dept. OSXA
3039 Cornwallis Road
Research Triangle Park, NC 27709
Phone: 919-543-8645
email: jaroden@us.ibm.com

ACES JOURNAL

EDITOR IN CHIEF

Atef Elsherbeni
EE Department, Anderson Hall
University of Mississippi
University, MS 38677
Phone: 662-915-5382
email: atef@olemiss.edu

NEWSLETTER ARTICLES AND VOLUNTEERS WELCOME

The ACES Newsletter is always looking for articles, letters and short communications of interest to ACES members. All individuals are encouraged to write, suggest or solicit articles either on a one-time or continuing basis. Please contact a Newsletter Editor.

AUTHORSHIP AND BERNE COPYRIGHT CONVENTION

The opinions, statements and facts contained in this Newsletter are solely the opinions of the authors and/or sources identified with each article. Articles with no author can be attributed to the editors or to the committee head in the case of committee reports. The United States recently became part of the Berne Copyright Convention. Under the Berne Convention, the copyright for an article in this newsletter is legally held by the author(s) of the article since no explicit copyright notice appears in the newsletter.

BOARD OF DIRECTORS

EXECUTIVE COMMITTEE

Osama Mohammed, President	Allen W. Glisson, Treasurer
Bruce Archambeault, Vice President	Richard W. Adler, Executive Officer
Keith Lysiak, Secretary	

DIRECTORS-AT-LARGE

Bruce Archambeault	2004	Allen W. Glisson	2005	Leo Kemple	2006
Andrzej Krawczyk	2004	Keith Lysiak	2005	Osama Mohammed	2006
Ray Perez	2004	Eric Mechielssen	2005	Tapan Sarkar	2006

ACES ELECTRONIC PUBLISHING GROUP

Atef Eisherbeni	Electronic Publication Managing Editor
Matthew J. Inman	Site Administrator
Jessica Drewrey	Assistant Administrator
Brad Baker	Contributing Staff
Imran Daker	Past Administrator
Chris Riley	Past Staff

Visit us on line at:
<http://aces.ee.olemiss.edu>

ACES Board of Directors Election Results 2003

Candidate statements appeared in the July 2003 ACES Newsletter.

Congratulations go to Randy Haupt, Juan R. Mosig, and Omar Ramahi.

These three newly elected Directors will be installed at the next Annual Meeting of the Members which occurs at the annual conference.

Rene Allard, Elections Committee Chair

DR. RANDY HAUPT



DR. JUAN R. MOSIG



DR. OMAR RAMAHI



CEM NEWS FROM EUROPE

Pat Foster

This year ACES (UK) devoted its one day meeting on September 22nd to Modeling Ships. 25 people turned up at Imperial College, London, for the event which was very lively.

The morning was devoted to a short course on the software package 'SHIP EDF' which has been developed by the Italian firm, IDS, based in PISA [1]. This is a major European package dealing with CEM modeling in all its forms for ships.

Tim Murphy who is head of Electromagnetics on the BAE Systems Ship team at Filton gave an over-view of problems in predicting EM performance on ships. He took as his example a Flight 1A Arleigh Burke Class destroyer which has a length of 155m and a beam of 20 mm. The frequency range of equipment is from 1 MHz to 18 GHz. He took three very different areas of prediction as examples. The first was an HF model which is treated with MoM techniques and is capable of identify hot spots around the ship so that operational constraints can be set at an early stage in the ship design. The second was a surveillance radar where he showed the volumes within which levels of 200v/m were exceeded. Again this enables operational constraints, particularly as regards helicopter safety, to be set well in advance. As a third example, he discussed below-decks equipment for de-gaussing where Vector Fields' TOSCA was used. This showed the crew must be protected. Tim Murphy pointed out that there was not much evidence around on the effects of long-term exposure of humans to such fields.

There was an interesting discussion on the use of electric motors for warships. These are coming into use for cruise ships where the release of internal space and the quietness is an attraction but there are serious problems in warship use.

The major presentation of the morning was from Stephano Chiti of IDS. The software package covers antenna installed performance, EMC and RCS and IR signatures. As you might expect, a great deal of the package is devoted to data management such as configuration control (dealing with the many different versions of any one ship design), a library of antennas and materials. The work flow for a single example was worked through. Clearly the amount of data required is very large and importing the ship geometry is a major exercise. Configuration control is required so that traceability is maintained. The IDS website [1] does contain some data on EDF. The methods employed are Method of Moments, Physical Optics and GTD. High gain antennas are modeled using electric and magnetic dipoles in front of a flat plate.

The output can be in the form of a Risk Assessment.

A major section of the course was devoted to validation and the accuracy required. There is the usual problem that, in comparing predictions with measurements, it is assumed that all the errors are in EDF. In the case of special measurements made as Funtington, DERA, UK, on a mock-up mast it could clearly be seen that the security fence was affecting radiation patterns. A large number of measurements were made in this trial on antenna patterns and coupling as well as field strength. These all showed the program to be as accurate as required by the customers. There was a discussion

on the setting of standards for agreement in that the accuracy required was +/- 4 dB over 0.0 to -20 dB below peak and some of the audience thought this should be related to dBi not relative decibels.

Future developments involve the incorporation of hybrid methods and some numerical experiments have been carried out using a mixed of MoM and PO on a dipole antenna near to two masts. These experiments range from a full MoM prediction to a prediction using MoM for the antenna alone and PO for the mast interactions which reduce the runtime from 41549 seconds to 839 seconds. The radiation patterns were clearly in error in the shadow region for the last method. Other developments would be the incorporation of a TLM approach to FSS materials and the modeling of layered materials.

This is a very powerful program which is slanted towards the systems aspects and intended to help the ship designers decide on details of the ship's structure and layout.

There was also a demonstration of EDF. The program operates on UNIX or NT and assumes that team operation is required by the customer – another reason for requiring careful configuration control. Multiple CPUs can be used when dealing with (say) HF antennas on the ship using MoM.

Several papers related to ship modeling were presented in the afternoon. These papers deserve a lengthy exposition for each one. All I shall do here is to list the papers so more detail can be obtained directly from the author

Waseem Qureshi, (Bae Systems ATC, Great Baddow, UK), 'EM modeling of the Sampson Radome'
M El Hachemi, (Swansea University, UK), 'Low-Order Method for Solving Electromagnetic Scattering Problems'

A J Keddie, Imperial College, London, UK, and M D Pocock (Frazer Nash Consultancy), 'Static Ship Signature Modeling'

A Duffy (de Montfort University, Leicester, UK), A Drozd (ANDRO Com Soltns, Rome, USA) and B Archambeault (IBM, NC, USA), 'Towards Validating CEM Modeling'

A J Cottee, M Rayner and C Parini, (QMW College, London, UK), 'Antenna Analysis using Discrete Green's Function FDTD Method'

S P Benham, J Lord (BAE Systems ATC, Gt Baddow) and J Burbage (BAE Systems, CDI, Filton, UK), 'Challenges in the CEM Modeling of Ships'

1. Website at www.ids-spa.it

The J-Pole Antenna

R.P. Haviland, W4MB
1035 Green Acres Circle, N.
Daytona Beach, Florida 32119

Editor's Note:

The following article had technical difficulties with the clarity of some of the plots. The softcopy of this article can be expanded so that these plots become clear. Interested parties may contact the author directly for clearer hardcopy plots if necessary.

The J-pole Antenna

R.P. Haviland, W4MB
1035 Green Acres Circle, N.
Daytona Beach, Florida 32119

I. INTRODUCTION

This study began as an Amateur Radio project. It is of interest here because it shows the necessity for considering both direct and field coupling of segments, gives some approaches to the drive impedance of end-fed antennas, and demonstrates some inherent limitations of analysis programs.

The J-pole antenna is mechanically simple, and gives good performance for the effort expended on its fabrication. As shown by Fig. 1, it can be constructed from a length of wire with two bends, although the more common VHF designs employ three pieces of tubing plus two 90° elbows. A J-pole can be built quickly from a piece of twin-lead or ladder line. In all cases, the standard feed method is to tap the two connections of the feed line part way up on the U-section, adjusting the position for minimum SWR.

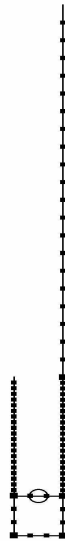


Fig. 1. Typical J-pole antenna, as prepared for Eznec analysis. Segmentation of the lower part of the U and the feed is typical.

II. STANDARD J-POLE DESIGN PRACTICE

The "standard" J-pole design calls for a U section one quarter-wavelength high, with the one extended section being an additional half-wavelength long. The SWR performance of such a design can be excellent, as shown in Fig. 2, which is for a 140 MHz J-pole made from half-inch copper tubing, with the U section spaced 2.0 inches on centers. This chart is for a

feed tap at 10% of the height of the U section. It assumes that the feed system is set to the resistance at the feed point, 11.12 Ω in this case. This gives an SWR of 1.05 at 140 MHz, with a 2:1 SWR bandwidth of nearly 6 MHz, more than ample to cover the 2-meter amateur band. Gain is 2.35 dBi, essentially that of a half-wave dipole. Note, however, that the azimuth pattern deviates from uniform (circularity) by just over 1 dB, and maximum gain is tilted upward by 8° in this case.

Inspection of Fig. 2 shows that the point of minimum SWR is at 140.2 rather than the design frequency 140.0 MHz. Also, the impedance at the feed point is well below the usual objective of 50 Ω . This means the tap point needs to be moved upward. The study reported here had the goal of understanding the J-pole characteristics well enough to achieve minimum SWR precisely at the design frequency and a 50 + j0 Ω feed point impedance. As will be seen, these objectives have not been completely realized. In this work, some of the limitations of antenna modeling were found to be significant.

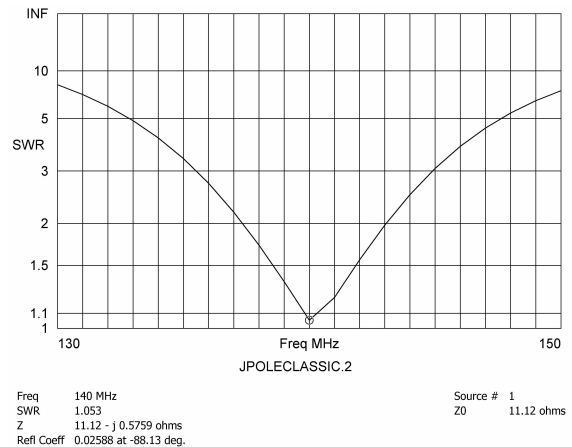


Fig. 2. SWR of a classical J-pole, with feed set to match 140 MHz resonance. The SWR bandwidth varies with mechanical design details, but is usually relatively wide.

Looking again at Fig. 1, it is evident that the antenna is composed of three coupled circuits. The first is the antenna radiating section, which has a natural frequency and a characteristic impedance, both functions of conductor diameter and length. This antenna is intentionally end-fed, directly voltage-coupled to one arm of the U impedance matching section (the second circuit) which theoretically transforms and infinite resistance at the open end to zero at the short. The third circuit, the feed, is then set to the value of desired feed resistance, usually 50 Ω .

The actual situation is far more complex than this simplistic

view. Fig. 3 shows some of the reason for the complexity. First, the NEC calculated current on the half-wave radiator does not follow the nearly free-space cosine curve of an antenna loosely coupled to the stub, shown in Fig. 3a, but when physically connected departs from this in magnitude near the junction to the U section, as shown in Fig. 3b. Also, not shown here, the phase along the antenna varies by some 120° , mostly close to the U section while phase variation is small on the upper half. Second, the currents on the two arms of the U section are not equal in magnitude. Further (also not shown in Fig. 3), the phase of the two currents is not the theoretical 180° as found on the stub alone, but varies along the U from 176° to 143° . Finally, there is a marked discontinuity in current at the feed point as the tap position is raised. There is a minor difference in amplitude and phase at the two ends of the feed.

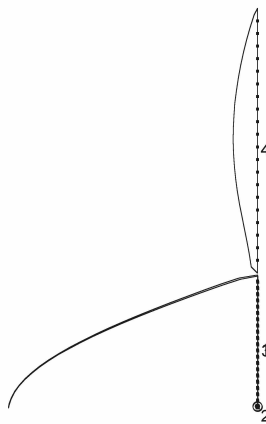


Fig. 3a

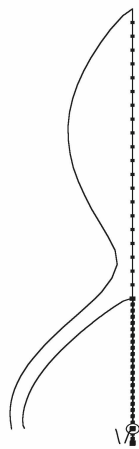


Fig. 3b

Fig. 3. Current distributions. (a) Antenna coupled to U section only by em fields, (b) Coupling by fields and direct connection. The position of minimum current in (b) varies as feed frequency varies.

Fig. 4 shows some explanation of these differences. This is a plot of the total near field at the level of the U-antenna junction, and a short distance away. Even with an excitation of only 12 Watts, the E-field intensity reaches 6000 V/m. The antenna, at zero on the y-axis, decreases the field intensity to

1000 V/m. The unconnected arm of the stub at 2 inches has a high intensity, but the maximum intensity is between the stub arms. Much greater resolution would be needed to define the precise location, but this has not seemed to be important.

It is evident that, in addition to the marked effect of the direct connection, there is a coupling between the U stud and the radiator through the field intensities of the stub and antenna. Also, while the stub arms form a transmission line, the coupling between them is affected by the presence of the antenna, and further by the feed connection. Net radiation from the unbalanced line causes the pattern distortion in the horizontal plane, and the non-symmetric current on the radiator causes the vertical plane pattern shift.

These effects appear to be inherent: they are relatively small, and have previously been ignored. It has not seemed worthwhile to correct them. However, there is the matter of locating the proper tap point for the drive feed and, in some installations, the need to secure unity SWR at the design frequency. The following is a report on the examination of attempting to develop a "cut and it's perfect" design approach. This turned out to be surprisingly difficult, and is not fully realized (see the recommendations at the end).

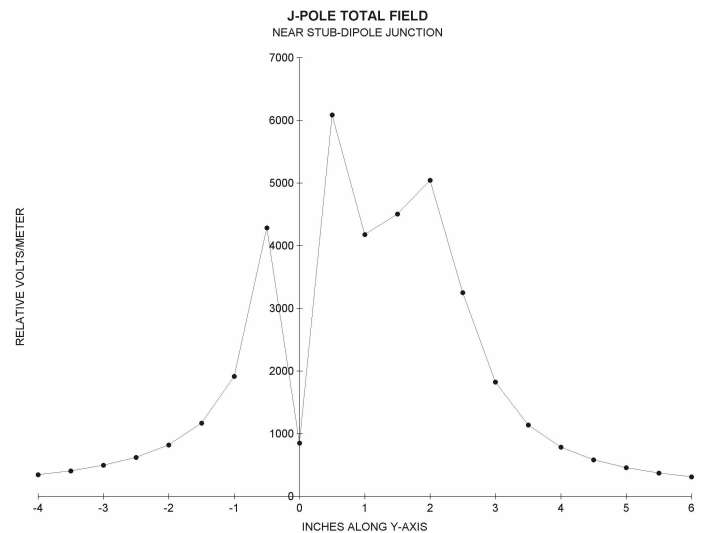


Fig. 4. E-field component of the near field close to the antenna and at the level of the antenna-U junction. The plane of the U is on the Y-axis. Maximum intensity is between the U arms, close to the side connected to the antenna. At approximately twice the U spacing from the arms, the field is nearly symmetrical.

III. CHARACTERISTICS OF THE STUB

Fig. 5 shows the major characteristics of the stub, considered separately. Fig. 5a shows the resonant frequency, measured by the point of zero reactance at the feed, as a function of conductor size, for a stub $\frac{\lambda}{4}$ at 150 MHz. Over this range it varies by less than $\pm 1\%$, negligible in most situations. The effect of mounting and nearby objects is probably greater. Note the slope changes in the curve. These do repeat in the

NEC calculations. However, they may be due to limits on the program. Warnings of segments being improper do occur in this analysis.

Fig. 5b shows the effect of varying the stub spacing, for a stub $\frac{\lambda}{4}$ high at 144 MHz. Over this range, the resonant frequency does vary linearly with spacing. However, if the total length of conductor is considered, the length of the two sides plus the length of the bottom connection, the resonant frequency is nearly a constant with total conductor length, to within just over $\pm 0.5\%$. The small departure ($< 0.003\lambda$) from $\frac{\lambda}{2}$ appears to arise from field fringing at the open stub ends. If stub correction is needed, the height can be set to give 0.4975λ as the total conductor length.

IV. CHARACTERISTICS OF THE ANTENNA

Information on end-fed antennas is almost non-existent. All I have seen use the approximation that the characteristics are that of half of a center-fed dipole. This neglects the effects of coupling between the two halves. Method-of-moments techniques such as implemented in NEC can approximate the end resistance by using a large number of segments, and deriving the drive resistance as the feed segment approaches the wire end, then extrapolating to total length. This is possibly adequate for thin wires, but with large diameter wires there will be an appreciable field from the wire (or tubing) end, which is neglected by all programs I have seen. The effect can be determined for very large conductors by simulating these as a grid of wires, closed at the ends by a radial grid. A conclusion to draw is that end-feed drive resistance is really not known. Further, the departure from a cosine current distribution in the J-pole case has an appreciable effect.

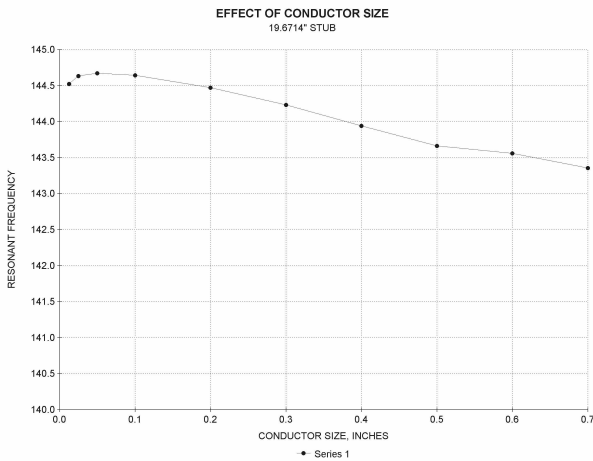


Fig. 5a

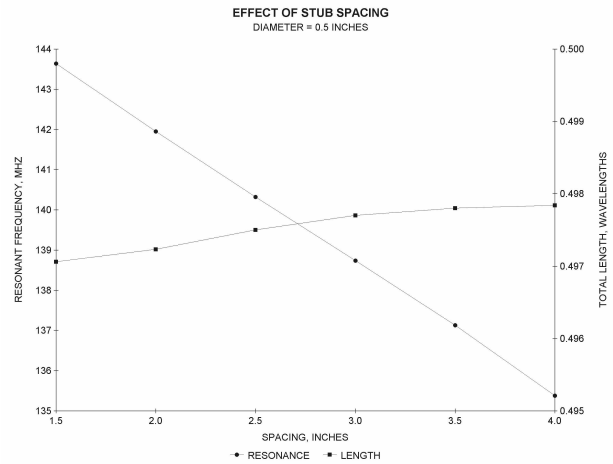


Fig. 5b

Fig. 5. Effect of dimension variation of a $\frac{\lambda}{4}$ stub. (a) Conductor diameter has a small effect on resonance, less than 1% of nominal frequency, (b) Resonant frequency is a linear function of U arm spacing, but is nearly independent of spacing for total length of conductor.

Fig. 6 shows calculated values of the J-pole antenna resistance and reactance. This assumes that the impedance measured for the J-pole assembly is the effect of two impedances in parallel, that of the stub and that of the antenna. The stub impedance was first determined with no antenna and the feed at the top of the stub, then recalculated with the antenna in place. Both resistance and reactance vary almost as the log of diameter over the selected range of sizes.

A number of attempts to visualize the mechanisms involved, and to find a reliable method of going from antenna parts to the complete antenna were made. They led to the further conclusion that it is necessary to work with the complete antenna, rather than attempting to handle it by sections.

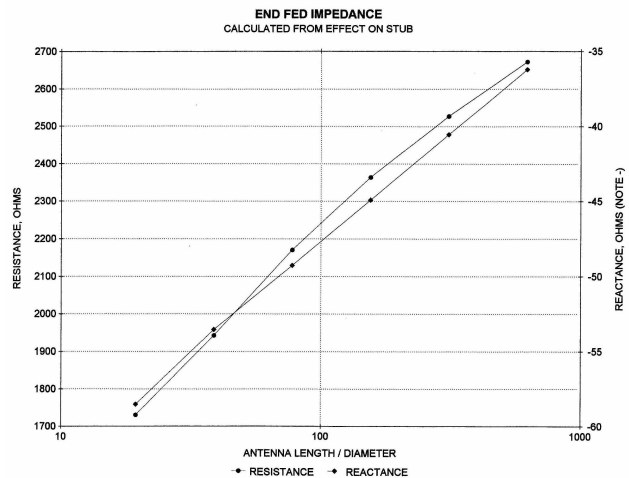


Fig. 6. Calculated end-feed impedance of a half-wave antenna used in the J-pole configuration. See text.

V. THE J-POLE ASSEMBLY

The drive impedance of a 142 MHz J-pole with stub 19.4" high and antenna extending to 58.8" is shown in Fig. 7 for drive positions up to 25% of stub height. Drive resistance varies from essentially zero to over 100Ω, with the variation being nearly linear with tap height. The height for a 50Ω feed is about 12% of stub height.

For tap positions below 10%, the drive reactance change with drive position is small. However, at greater tap heights, the reactance is also increasing, again nearly linearly with height. It appears that this is due to the small inductance inherent in the tap connection: its effect becomes larger as the voltage on the stub increases with height (very nearly a cosine function). This is a complication in matching. It means that there are conditions where increasing tap height to increase drive point resistance is also detuning the system, which requires some further adjustment.

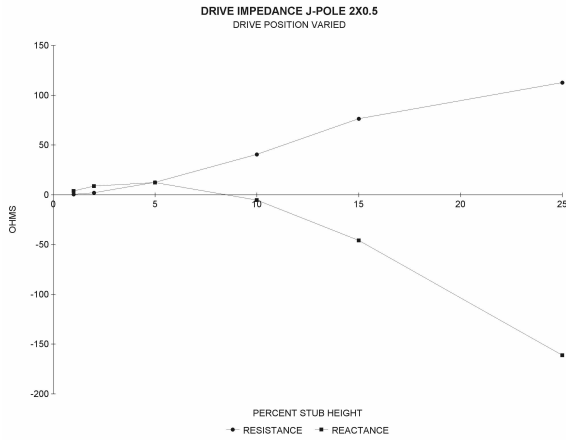


Fig. 7. Drive impedance of a J-pole assembly as the feed position is varied. If the feed is higher than about 10% of the U height, both drive resistance and reactance change. Most designs place the feed in the area of low reactance change.

But there are further complexities. Fig. 8a shows the effect of antenna length on drive impedance. The drive resistance varies much more than the reactance. Again, change to adjust one quantity changes another. Essentially the same situation occurs as the frequency is changed, as shown by Fig. 8b. Finally, as shown in Fig. 8c, changing the conductor size (of both stub and antenna) has a marked effect on drive resistance, but little on reactance. The major reactance change is for small conductors, where the field fringe effects at the top of the stub are relatively large.

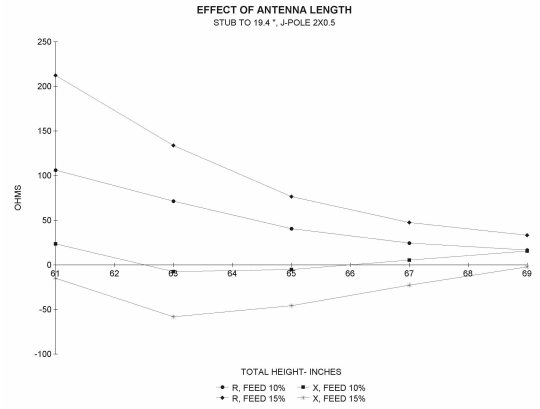


Fig. 8a

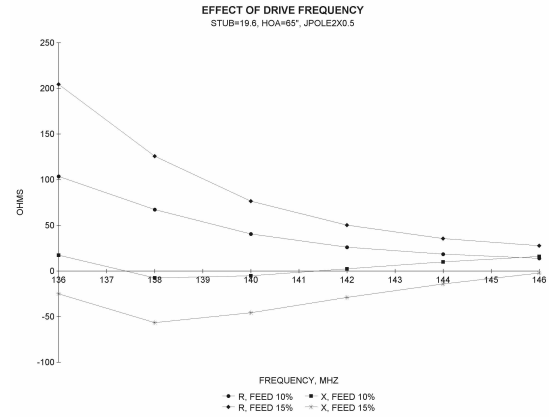


Fig. 8b

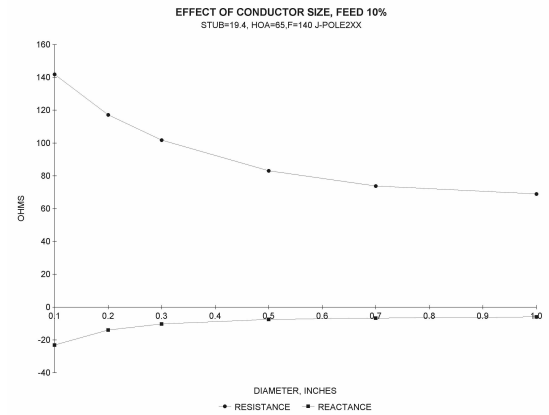


Fig. 8c

Fig. 8. Variational effects on a J-pole assembly. (a) Effect of varying the antenna length on drive resistance, for four feed positions, (b) Effect of varying operating frequency, and (c) Effect of varying diameter of antenna section only. The effects of changing antenna length and drive frequency are very nearly the same. Antenna diameter has little effect on drive point reactance.

VI. RECOMMENDATIONS FOR DESIGN

Given these interactions, it has not been possible to develop a "cut, assemble and it works perfectly" approach to securing

exact match at a given design frequency. This leads to the following recommendations:

- If 1.0 SWR at a given frequency is not a necessity, use the classical $\frac{\lambda}{4}$ stub and $\frac{\lambda}{2}$ antenna dimensions. The tap position can be set using Fig. 9. Note that this will not be the $50 + j0$ drive point, but the one where the magnitude of Z is 50 Ohms.
- If a better match is a necessity, model the antenna with a NEC program, changing dimensions by trial until the design goal is reached. Figures 7 and 8 can be used to give the direction of change, and the approximate amount.
- If exact match is a goal with an antenna already built, measure the drive impedance with a meter or bridge giving both R and X values. Adjust the tap position to give the goal drive resistance, most often 50 Ohms. Use the curves or equations in the *ARRL Antenna Handbook* to design an open or shorted stub to cancel the reactance.

Probably, the classical design will be entirely adequate.

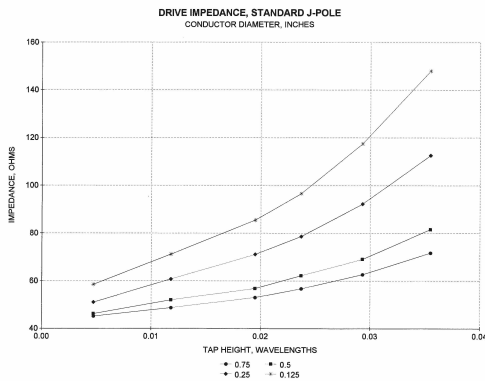


Fig. 9. Drive point impedance of a classical J-pole as a function of tap position, for four system conductor diameters. Interpolate for other diameters. The indicated position should give a good match.

VII. J-POLE VARIATIONS

There are variations of a J-pole, created by adding another half-wave antenna above the main radiator, using either a quarter-wave stub or resonant LC parallel trap as shown in Fig. 10a to give the necessary phase reversal. Be cautious in using this design. For example, Fig. 10b shows the pattern for the antenna of Fig. 10a, using a resonant trap. The gain has increased to 3.5 dB, but the lobe has been tilted upward, so the gain in the horizontal plane has actually decreased. This is partly due to the loss along the wire which happens with all end-fed antennas, but is largely due to the fact that the two half-wave sections are only coupled through the radiation field. Using a quarter-wave stub instead reduces the upward beam tilt. In trials here, the increase in horizontal gain was only on the order of 1 dB, hardly worthwhile.

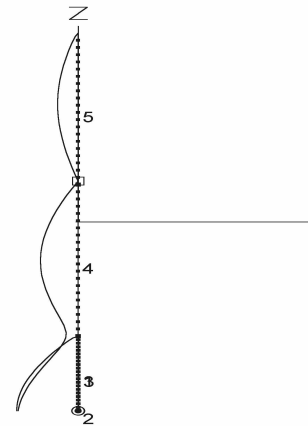


Fig. 10a

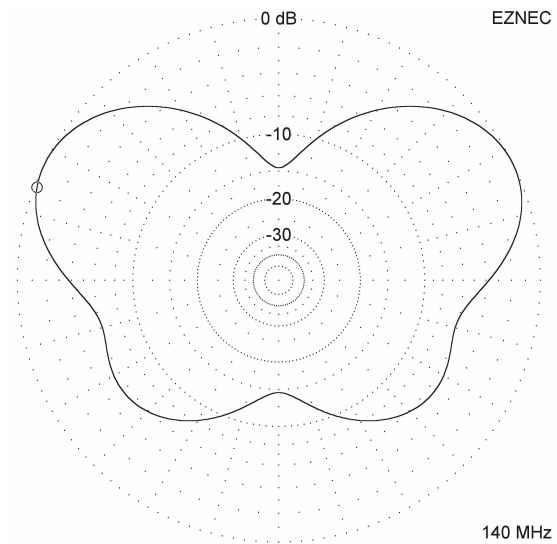


Fig. 10b

Fig. 10. A J-pole version with two colinear antenna elements, in this case separated by a resonant trap. (a) Current distribution, and (b) Pattern in the vertical plane of a vertical assembly. The current in the upper antenna will be greater if the trap is replaced by a quarter-wave stub, and maximum radiation will be at a lower elevation angle.

There is a way to secure both a better pattern and better gain. This, in essence, mounts a second J-pole upside down from the common design, as shown in Fig. 11a. Here, the feed is at the base of the U of either antenna to give pattern symmetry. The antenna is really constructed of two pipe sections one wavelength long, overlapping by a half-wave, and fed at the line of symmetry.

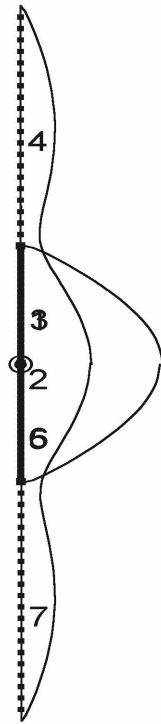


Fig. 1. Fig. 11b

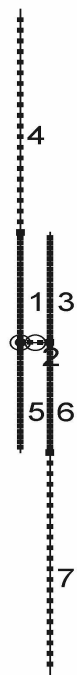


Fig. 11a

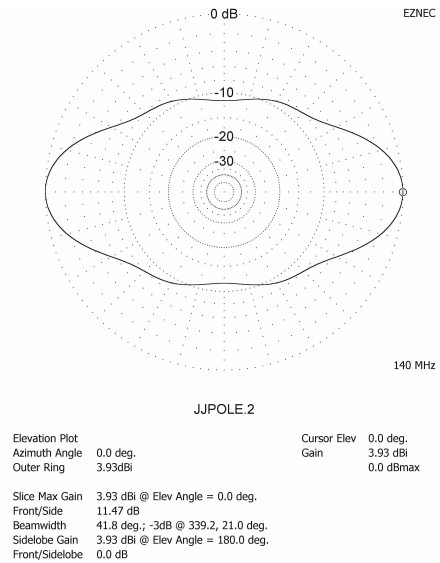


Fig. 11c

Fig. 11. Two J-poles in a back-to-back configuration, formed from two 1λ conductors overlapping a half-wavelength, fed at the center of symmetry. (a) Schematic, (b) Current distribution, and (c) Vertical plane pattern. This is a simple way to increase gain.

The current on the antenna is shown in Fig. 11b. While the currents on the two stub sections are not the same, otherwise the distribution is symmetrical. The result of this shows in the pattern plot of Fig. 11c. Gain has nearly doubled, essentially to 4 dB. The maximum gain is at right angles to the line of the antennas, that is, toward the horizon. Since the feed is to the bottom of two U sections in parallel, the drive resistance is very low, on the order of 7Ω . The point of zero drive reactance is much lower than indicated by the half-wave section length, being very close to 0.44 wavelengths. Design parameters for this variation were not studied further.

Mounting this antenna as an isolated vertical may be a little more of a problem than for the conventional type. However, it is easy to mount from the corner of a tower by the use of one or two plastic tube standoffs plus one or two tee-sections and element spacers. Feed would be at the center of symmetry, with a quarter-wave matching transformer (which could be integrated with the supports) to change the low drive resistance of 6.8Ω to the transmission line impedance. This design merits more attention.

VIII. CONCLUDING REMARKS

The mechanically simple J-pole antenna proved to be surprisingly complex, partly due to the presence of three coupled circuits, but also to the fact that common construction requires approaching the computational limits of NEC.

The author found it quite surprising that the “standard design” 0.25λ and 0.5λ J-pole sections (as discussed in Section II) turn out to be so close to best design, after experience with the difference in quads and dipoles.

Implementing the Locally-Corrected Nyström Method

Stephen D. Gedney
Department of Electrical and Computer Engineering
University of Kentucky
Lexington, KY 40506-0046

I. Introduction

The focus of this tutorial is to detail the implementation of a locally corrected Nyström (LCN) based solution of three-dimensional electromagnetic scattering problems. The LCN method has demonstrated exponentially convergent solutions for electromagnetic scattering problems, including problems involving PEC scatterers [1, 2], dielectric scatterers using surface [3] and volume integral equation methods [4], as well as for thin-wire antennas [5]. The principal advantages of employing a methodology that is high-order convergent are: *i*) the computer resources required to realize accuracy to a desired tolerance can be greatly reduced as compared to a classical low-order technique, *ii*) accurate estimations of the solution error can be efficiently obtained, and *iii*) the LCN method is quite simple to implement. As the LCN method is maturing it is being applied to more practical engineering design problems and is proving to be a very powerful solution technique.

The following sections of this tutorial are aimed at outlining more specific details of implementing the LCN method. While space limits a full description of all aspects of an implementation, it is hoped that enough detail is provided to encourage readers to implement and test this very powerful solution technique.

II. Integral Equations

Consider the interaction of a time-harmonic electromagnetic wave ($e^{j\omega t}$ time-dependence) with a material scatterer made of a composite of penetrable materials (with piecewise constant material profiles) and non-penetrable conductors. Let the i^{th} region with material profile (ϵ_i, μ_i) be defined as volume V_i . A surface separating volumes V_i and V_j is denoted as $S_{i,j}$. Let $S_{i,j}^+$ denote the surface just inside V_i , and $S_{i,j}^-$ denote the surface just inside V_j . Equivalent current densities are then placed on surfaces separating each material volume. These are defined as:

$$\vec{J}_{i,j}^+ = \hat{n}_i \times \vec{H} \Big|_{S_{i,j}^+}, \quad \vec{M}_{i,j}^+ = -\hat{n}_i \times \vec{E} \Big|_{S_{i,j}^+}, \quad \vec{J}_{i,j}^- = \hat{n}_j \times \vec{H} \Big|_{S_{i,j}^-}, \quad \vec{M}_{i,j}^- = -\hat{n}_j \times \vec{E} \Big|_{S_{i,j}^-}, \quad (1)$$

where \hat{n}_i and \hat{n}_j are the unit normal directed into V_i and V_j , respectively. At any point on $S_{i,j}$ $\hat{n}_j = -\hat{n}_i$, and the tangential fields are continuous, thus:

$$\vec{J}_{i,j}^+ = -\vec{J}_{i,j}^- = \vec{J}_{i,j}, \quad \vec{M}_{i,j}^+ = -\vec{M}_{i,j}^- = \vec{M}_{i,j}. \quad (2)$$

On the surface of a perfect conductor, only the electric current density is supported. Thus,

$$\vec{J}_{i,p} = \hat{n}_i \times \vec{H} \Big|_{S_{i,p}^+}. \quad (3)$$

The scattered electric and magnetic fields radiated by the equivalent currents in volume V_i are computed as:

$$\vec{E}_i^{scat}(\vec{J}_{eq}, \vec{M}_{eq}) = \eta_i \mathbf{L}_i(\vec{J}_{eq}) - \mathbf{K}_i(\vec{M}_{eq}), \quad (4)$$

$$\vec{H}_i^{scat}(\vec{J}_{eq}, \vec{M}_{eq}) = \mathbf{K}_i(\vec{J}_{eq}) + \eta_i^{-1} \mathbf{L}_i(\vec{M}_{eq}), \quad (5)$$

where

$$\mathbf{L}_i(\vec{X}_{eq}) = -jk_i \int_{\Omega} \left[\bar{\bar{I}} + \frac{1}{k_i^2} \nabla \nabla \right] \cdot \vec{X}_{eq}(\vec{r}') G_i(\vec{r}, \vec{r}') d\Omega', \quad (6)$$

$$\mathbf{K}_i(\vec{X}_{eq}) = \int_{\Omega} \nabla G_i(\vec{r}, \vec{r}') \times \vec{X}_{eq}(\vec{r}') d\Omega', \quad (7)$$

and Ω is either a surface or volume, $\bar{\bar{I}}$ is the unit dyad, $G_i(\vec{r}, \vec{r}') = e^{-jk_i|\vec{r}-\vec{r}'|} / 4\pi|\vec{r}-\vec{r}'|$, $k_i = \omega\sqrt{\epsilon_i\mu_i}$ and $\eta_i = \sqrt{\mu_i/\epsilon_i}$.

A surface integral formulation is then derived by enforcing the appropriate constraints on each material boundary. A combined field formulation based on Müller's formulation [6, 7] is applied on material surfaces leading to:

$$\vec{t} \cdot \epsilon_r \vec{E}_i^{inc} \Big|_{S_{i,j}^+} + \vec{t} \cdot \epsilon_r \vec{E}_j^{inc} \Big|_{S_{i,j}^-} = \vec{t} \cdot \hat{n}_i \times \vec{M}_{i,j}(\epsilon_{r_i} + \epsilon_{r_j}) - \vec{t} \cdot \epsilon_{r_i} \vec{E}_i^{scat} \Big|_{S_{i,j}^+} - \vec{t} \cdot \epsilon_{r_j} \vec{E}_j^{scat} \Big|_{S_{i,j}^-}, \quad (8)$$

$$\vec{t} \cdot \mu_r \vec{H}_i^{inc} \Big|_{S_{i,j}^+} + \vec{t} \cdot \mu_r \vec{H}_j^{inc} \Big|_{S_{i,j}^-} = -\vec{t} \cdot \hat{n}_i \times \vec{J}_{i,j}(\mu_{r_i} + \mu_{r_j}) - \vec{t} \cdot \mu_{r_i} \vec{H}_i^{scat} \Big|_{S_{i,j}^+} - \vec{t} \cdot \mu_{r_j} \vec{H}_j^{scat} \Big|_{S_{i,j}^-}, \quad (9)$$

where, \vec{E}_i^{inc} , \vec{H}_i^{inc} are radiated by impressed sources in region i , \vec{E}_i^{scat} , \vec{H}_i^{scat} are radiated by equivalent currents in volume V_i , and \vec{t} is a test vector tangential to $S_{i,j}$. The advantage of this formulation over the classical PMCHWT (Poggio, Miller, Chang, Harrington, Wu and Tai) formulation [8] is that it behaves as a second-kind integral equation moderate to low contrast materials, and the hyper-singularity of the \mathbf{L} -operator in (6) is reduced by one order.

On a PEC surface, the combined field integral equation (CFIE) is applied [9]:

$$\frac{\alpha}{\eta_i} \vec{t} \cdot \vec{E}_i^{inc} \Big|_{S_{i,p}} + (1-\alpha) \vec{t} \cdot \hat{n}_i \times \vec{H}_i^{inc} \Big|_{S_{i,p}} = \frac{\alpha}{\eta_i} \left(-\vec{t} \cdot \vec{E}_i^{scat} \Big|_{S_{i,p}} \right) + (1-\alpha) \vec{t} \cdot \left(\vec{J}_{i,p} - \hat{n}_i \times \vec{H}_i^{scat} \Big|_{S_{i,p}} \right). \quad (10)$$

where α is a real constant, generally defined between 0 and 1.

III. Nyström Discretization

In [2], it was shown that the LCN method is equivalent to a moment method formulation with smooth basis and testing functions that employs a fixed-point numerical quadrature approximation for the outer integral. Through a simple transformation, this can identically be expressed as a quadrature-point matched method of moment formulation [10]. Then, mapping the currents to the quadrature points, the method of moment formulation can then be rendered in

an identical form as the LCN method [2]. Since most practitioners in computational electromagnetics (CEM) are trained in the method of moments, this paradigm will be followed in this tutorial.

It is assumed that the three-dimensional surfaces are discretized using high-order quadrilateral patches (Section IV). A set of basis functions is then introduced for each patch. For smooth surfaces, one can expand the vector surface current density in terms via Legendre polynomials [1, 2, 10] leading to a set of functions that is polynomial complete to order p :

$$\begin{aligned}\vec{J}_i^{j,k}(u^1, u^2) &= \vec{a}_i P_j(u^1) P_k(u^2) / \sqrt{g}, \\ \vec{M}_i^{j,k}(u^1, u^2) &= \vec{a}_i P_j(u^1) P_k(u^2) / \sqrt{g},\end{aligned}\tag{11}$$

for $(i=1,2; j,k=0..p-1)$, where, following the notation of Stratton [11], (u^1, u^2) are the local curvilinear coordinates of the quadrilateral patch, \vec{a}_i are the local unitary vectors and \sqrt{g} is the Jacobian evaluated at (u^1, u^2) , and $P_j(u)$ are j^{th} -order Legendre polynomials. Note that for simplicity, we have assumed identical basis orders along the u^1 and u^2 directions. In general, these do not have to be equal. Some observations are made for this choice of basis: 1) the basis functions are local to each quadrilateral patch and do not enforce current continuity across patch boundaries, 2) the i -th basis is directed along \vec{a}_i and is tangential to the patch boundaries $u^j = 0$ and $u^j = 1$ ($j \neq i$), and 3) there are $2 \times p^2$ basis functions per patch for each current type.

For geometries that lead to currents with known edge singularities (say a knife edge), basis functions with Jacobi polynomials can also be employed [2, 12]. Else, for general edge singularities, a mixed-order basis proposed by Çalişkan and Peterson can be employed [13, 14]. For the sake of this tutorial, we will limit the discussion to the polynomial complete basis in (11).

The currents in the integral operators in (8)-(10) are expanded via the basis functions in (11) and weighted by constant coefficients. This leads to $2 \times p^2$ unknowns per patch for each current type. Consequently, $2 \times p^2$ constraints must be enforced. To this end, an appropriate quadrature rule is introduced over each quadrilateral patch. For a quadrilateral patch, a convenient choice is the product of two p -point one-dimensional Gauss-Legendre quadrature rules [15]. This leads to p^2 abscissa points on the patch. Then, the integral operator is “tested” by performing the inner-dot product of the operator with a test vector at each of the quadrature abscissa points. A convenient choice for the test vector is simply the unitary vectors \vec{a}_i . On a material surface, the same testing procedure is used for the electric field integral equation (EFIE) and the magnetic field integral equation (MFIE) in (8) and (9), respectively. Thus, for each field type, there are a total of $2 \times p^2$ constraints per patch. This leads to a square linear system of equations.

IV. High-Order Patch-Based Discretization

As found in [1, 2], the LCN method is most efficient when employing higher-order basis on large smooth curvilinear patches – that is, the error will converge to a desired accuracy with fewer unknowns. The reason for this is simple: higher-order basis converge more rapidly than lower order basis. Thus, with the LCN method it is desirable to model geometries with large curvilinear cells that represent the surface to sufficient accuracy. A balance of CPU time and memory is often realized with a discrete patch representation that has an average cell radius of

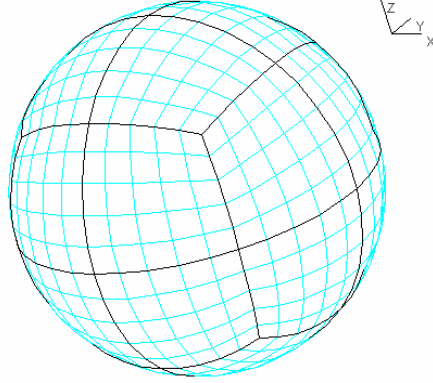


Fig. 1. Curvilinear quadrilateral cell discretization of a spherical surface with 24, 5th-order cells).

$\sim 1 \lambda$. Thus, it becomes imperative to employ isoparametric curvilinear patches that accurately model a surface of arbitrary curvature. If one can not support such patches, then one is forced to use a refined discretization – thus losing the advantage of the high-order method. For classical low-order techniques, this has not been an issue since the slow convergence requires one to resolve the surface with a minimum of 10 to 20 edges per linear wavelength to get reasonable accuracy. Often, such fine sampling is also enough to represent a curved surface to sufficient accuracy using a piecewise linear approximation.

Most commercial mesh generation programs are limited by the order of curvilinear cells that can be generated. Most CAD packages provide at least bi-linear quadrilaterals (first order). Some will render bi-quadratic and very few will render up to bi-cubic elements. This is still too limiting, since arbitrary order is desirable for a high-order method. To have this ability, we have developed a mesh tool that will generate quadrilateral elements of arbitrary order from an initial coarse linear discretization. As an example, Fig. 1 illustrates a sphere that is approximated by 24 fifth-order quadrilateral patches that was generated by our mesh tool.

A quadrilateral patch of order n is represented by $(n+1) \times (n+1)$ nodes that lie on the surface. In the unitary space, these nodes are uniformly spaced, as illustrated in Fig. 2. Each node has a physical coordinate $\vec{r}_{j,k}$ ($j, k = 0, n$). The position at any arbitrary coordinate (u^1, u^2) can be obtained via interpolation:

$$\vec{r}(u^1, u^2) = \sum_{k=0}^n \sum_{j=0}^n \Phi_j^n(u^1) \Phi_k^n(u^2) \vec{r}_{j,k} \quad (12)$$

where the interpolation polynomials are expressed as:

$$\Phi_i^n(u) = R_i(n, u) R_{n-i}(n, 1-u) \quad (13)$$

where $R_i(n, u)$ is a Sylvester interpolation polynomial [16]:

$$R_i(n, u) = \begin{cases} \frac{1}{i!} \prod_{k=0}^{i-1} (nu - k), & 1 \leq i < n \\ 1, & i = 0 \end{cases} \quad (14)$$

It is noted that this interpolation procedure exactly represents a bi-linear quadrilateral when $n=1$, bi-quadratic quadrilateral when $n=2$, and a bi-cubic quadrilateral when $n=3$. It also represents interpolations to arbitrary order.

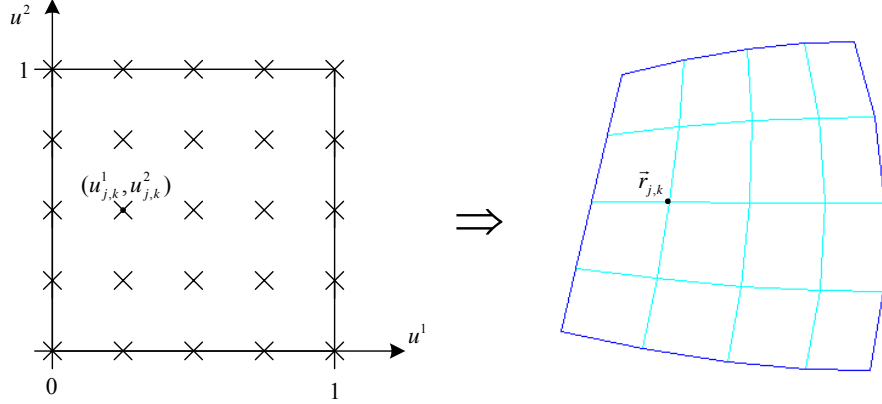


Fig. 2. Mapping of a fourth-order quadrilateral cell from the unitary space to the physical patch.

The unitary vectors for the patch are then computed as:

$$\vec{a}_i = \frac{\partial \vec{r}(u^1, u^2)}{\partial u^i} = \frac{\partial}{\partial u^i} \sum_{k=0}^n \sum_{j=0}^n \Phi_j^n(u^1) \Phi_k^n(u^2) \vec{r}_{j,k} \quad (15)$$

Analytical expressions for the derivatives of the interpolation polynomials are easily derived, and the derivatives of the Sylvester interpolation polynomials can be expressed via a recursive relationship that is efficiently computed.

This scheme is general enough to interpolate surfaces up to arbitrary order. However, it still must be realized that the interpolation scheme is only C^0 continuous. And, for very high-orders ($\sim n > 10$) the interpolation operator can be ill conditioned. As a result, Gibb's phenomena can occur leading to small high spatial-frequency oscillation of the interpolated surface. These issues can be resolved by working with interpolation functions that enforce higher degrees of continuity across patch boundaries (e.g., splines or NURBS) and possibly using non-uniform point sampling that minimizes the determinant of the Vandermonde matrix (e.g., Lobatto or Chebyshev point sampling). Nevertheless, the interpolation scheme proposed in (12) works quite well to reasonably high order.

In a general implementation of a method of moment code, one would like to use an object-oriented approach such that kernel evaluations are essentially independent of the patch type or order. That is, one would like to use the same code for bi-linear quads, high-order quads, or specific curvilinear patches that exactly conform to a canonical surface (e.g., spherical, conical, cylindrical, or ellipsoidal surfaces). This is easily done by defining a class (or a function) that simply returns the position vector and the unitary vectors given the local curvilinear coordinates (u^1, u^2) for the source or field patch. In this way, the kernel of the code has no direct dependencies on the source or field patch types.

V. Numerical Integration Issues

The operators defined in (4)-(10) require the computation of a convolutional integral performed over an arbitrary "source" patch and computed to a field point. This convolution is estimated using numerical integration. How this integration is computed will depend upon the separation of the field quadrature point and the source patch and the level of accuracy desired. If the field point lies on the source patch, then the kernel is singular and must be treated specially. If the field point is close to the source patch, then the integration must be performed using some

type of adaptive numerical quadrature. In general, if d digits of accuracy is expected from the final solution, then d -digits of accuracy should be demanded from the adaptive quadrature routine. This defines the “near” region. Adaptive quadrature is not needed once the field point is sufficiently far away that the fixed-point quadrature rule of the Nyström discretization provides at least d -digits of accuracy. This defines the “far” region. In the near region, adaptive quadrature is used to compute the convolutional integral to d -digits of accuracy. Then, a local correction is performed that effectively maps the current coefficient vector to the currents at the quadrature points (c.f., Sections II and III, pp. 2402-2404 of [2]). In the far region this leads to the single point-to-point reaction that is equivalent to estimating the numerical integration of the convolutional integral with a fixed-point quadrature rule.

The most difficult integration to perform in the near region is the singular integrations. The \mathbf{L} operator has a hypersingularity and must be properly manipulated so that it is numerically tractable. The \mathbf{K} operator has an integrable $1/R$ singularity. However, care still must be taken to compute this in an efficient manner.

Initially, consider the treatment of the \mathbf{L} operator. Specifically, from (6)

$$\vec{t}_m \cdot \mathbf{L}_i(\vec{J}_n) = -jk_i \left[\vec{t}_m \cdot \int_{s'} \vec{J}_n(\vec{r}') G_i(\vec{r}_m, \vec{r}') ds' + k_i^{-2} \vec{t}_m \cdot \nabla \int_{s'} (\nabla G_i(\vec{r}_m, \vec{r}') \cdot \vec{J}_n(\vec{r}')) ds' \right] \quad (16)$$

where, $\vec{J}_n(\vec{r}')$ is the vector basis function in (11), \vec{r}_m is an abscissa point of the quadrature rule on the field patch, and the test vector \vec{t}_m is evaluated at \vec{r}_m . The integrand of the first integral in (16) has a $1/R$ singularity. However, due to the double ∇ operator, the integrand of the second integral is hypersingular in the limit $R \rightarrow 0$. In fact, it exhibits a singularity of $\mathcal{O}(1/R^3)$.

Consequently, this term must be manipulated to reduce the order of singularity. Thus, we will focus on manipulating this term. Initially, the following identity can be derived:

$$\begin{aligned} \int_S \vec{t}_m \cdot \nabla \left((\nabla G_i(\vec{r}_m, \vec{r}') \cdot \vec{J}_n(\vec{r}')) \right) ds' &= - \int_S (\vec{t}_m \cdot \nabla) \left(\vec{J}_n(\vec{r}') \cdot \nabla'_{\parallel} \right) (G_i(\vec{r}_m, \vec{r}')) ds' \\ &= - \int_S \left(\vec{J}_n(\vec{r}') \cdot \nabla'_{\parallel} \right) (\vec{t}_m \cdot \nabla) (G_i(\vec{r}_m, \vec{r}')) ds', \end{aligned} \quad (17)$$

where we have made use of the reciprocal nature of the Green function such that $\nabla G_i(\vec{r}_m, \vec{r}') = -\nabla' G_i(\vec{r}_m, \vec{r}')$ and the complimentary nature of the operators $(\vec{J}_n(\vec{r}') \cdot \nabla'_{\parallel})(\vec{t}_m \cdot \nabla)$. Also, ∇'_{\parallel} is the projection of the gradient operator onto the surface tangent. Next, utilizing a vector identity, the right-hand-side of (17) is rewritten as

$$= - \int_S \nabla'_{\parallel} \cdot \left[\vec{J}_n(\vec{r}') (\vec{t}_m \cdot \nabla G_i(\vec{r}_m, \vec{r}')) \right] ds' + \int_S \nabla'_{\parallel} \cdot \vec{J}_n(\vec{r}') (\vec{t}_m \cdot \nabla G_i(\vec{r}_m, \vec{r}')) ds'. \quad (18)$$

The first term on the right-hand-side of (18) can be rewritten using the divergence theorem for open surfaces [1] as:

$$- \int_S \nabla'_{\parallel} \cdot \left[\vec{J}_n(\vec{r}') (\vec{t}_m \cdot \nabla G_i(\vec{r}_m, \vec{r}')) \right] ds' = - \int_C (\hat{e}' \cdot \vec{J}_n(\vec{r}')) (\vec{t}_m \cdot \nabla G_i(\vec{r}_m, \vec{r}')) dl' \quad (19)$$

where C is the closed contour bounding the open surface S , and \hat{e}' is the outward normal to the contour that is also tangential to the surface (i.e., $\hat{e}' dl' = d\vec{l}' \times \hat{a}_n$, where \hat{a}_n is the outward normal to S). Next, the second-term on the right-hand-side of (18) is rewritten as:

$$\int_S \left(\nabla_{\parallel}' \cdot \vec{J}_n(\vec{r}') \right) \left(\vec{t}_m \cdot \nabla G_i(\vec{r}_m, \vec{r}') \right) ds' = \int_S \nabla G_i(\vec{r}_m, \vec{r}') \cdot \left[\vec{t}_m \nabla_{\parallel}' \cdot \vec{J}_n(\vec{r}') \right] ds' \quad (20)$$

This term still has a singularity which is $\mathcal{O}(1/R^2)$. To reduce this by one order, the right-hand-side of (20) is rewritten as:

$$= \int_S \nabla G_i(\vec{r}_m, \vec{r}') \cdot \left[\vec{t}_m \nabla_{\parallel}' \cdot \vec{J}_n(\vec{r}') - \vec{K}_{mn}(\vec{r}') \right] ds' + \int_S \nabla G_i(\vec{r}_m, \vec{r}') \cdot \vec{K}_{mn}(\vec{r}') ds' \quad (21)$$

where, $\vec{K}_{m,n}(\vec{r}')$ is defined by

$$\vec{K}_{mn}(\vec{r}') = \frac{\vec{\Psi}_m(\vec{r}')}{\sqrt{g'}} \chi_{n,m}, \quad (22)$$

where $\chi_{n,m}$ is the constant:

$$\chi_{n,m} = \left(\sqrt{g'} \nabla_{\parallel}' \cdot \vec{J}_n(\vec{r}') \right) \Big|_{\vec{r}'=\vec{r}_m}, \quad (23)$$

and the vector $\vec{\Psi}_m(\vec{r}')$ is defined by:

$$\vec{\Psi}_m(\vec{r}') = \left(\vec{t}_m \cdot \vec{a}^1 \right) \Big|_{\vec{r}'=\vec{r}_m} \vec{a}_1(\vec{r}') + \left(\vec{t}_m \cdot \vec{a}^2 \right) \Big|_{\vec{r}'=\vec{r}_m} \vec{a}_2(\vec{r}') \quad (24)$$

such that at the singular point $\vec{K}_{mn}(\vec{r}_m) = \vec{t}_m \nabla_{\parallel}' \cdot \vec{J}_n(\vec{r}') \Big|_{\vec{r}'=\vec{r}_m}$. Consequently, the singularity in the first term on the right-hand side of (21) is simply $\mathcal{O}(1/R)$ and is numerically tractable. The second term in (21) can be simplified to:

$$\begin{aligned} \int_S \nabla G_i(\vec{r}_m, \vec{r}') \cdot \vec{K}_{mn}(\vec{r}') ds' &= - \int_S \left[\nabla_{\parallel}' \cdot \left(\vec{K}_{mn}(\vec{r}') G_i(\vec{r}_m, \vec{r}') \right) - G_i(\vec{r}_m, \vec{r}') \nabla_{\parallel}' \cdot \vec{K}_{mn}(\vec{r}') \right] ds' \\ &= - \oint_C \hat{e}' \cdot \vec{K}_{mn}(\vec{r}') G^R(\vec{r}_m, \vec{r}') dl' \end{aligned} \quad (25)$$

However, from (22)-(24), it is immediately seen that $\nabla_{\parallel}' \cdot \vec{K}_{m,n}(\vec{r}') = 0$. Then, applying the open surface divergence theorem on the remaining term:

In summary, from (17)-(25):

$$\begin{aligned} \vec{t}_m \cdot \nabla \int_S \left(\nabla G_i(\vec{r}_m, \vec{r}') \cdot \vec{J}_n(\vec{r}') \right) ds' &= + \int_S \nabla G_i(\vec{r}_m, \vec{r}') \cdot \left[\vec{t}_m \nabla_{\parallel}' \cdot \vec{J}_n(\vec{r}') - \vec{K}_{mn}(\vec{r}') \right] ds' \\ &\quad - \oint_C \left(\hat{e}' \cdot \vec{J}_n(\vec{r}') \right) \left(\vec{t}_m \cdot \nabla G_i(\vec{r}_m, \vec{r}') \right) dl' - \oint_C \hat{e}' \cdot \vec{K}_{mn}(\vec{r}') G_i(\vec{r}_m, \vec{r}') dl'. \end{aligned} \quad (26)$$

It is assumed that the Nyström discretization points are interior to S and do not lie on the contour C . Consequently, the surface integration in (26) and the leading term in (16) have an integrable

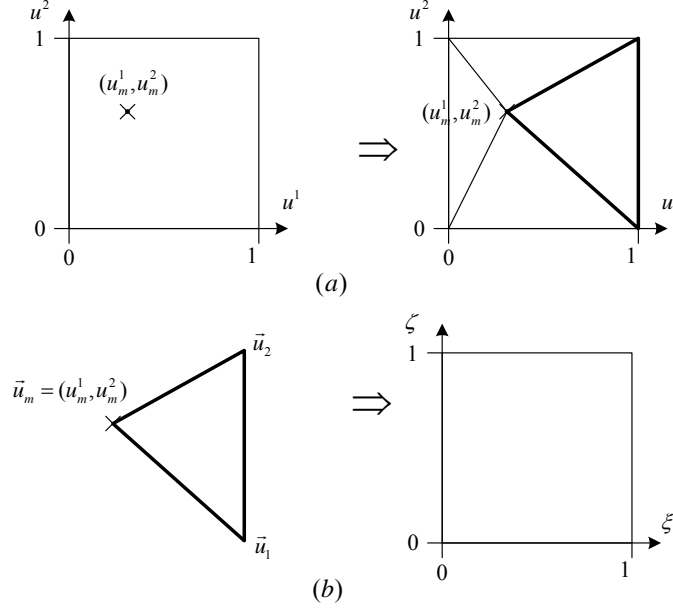


Fig. 3 (a) Decomposing the unitary square into triangles with common vertex at the singular point. (b) Mapping the ‘‘Duffy-triangle’’ into a parameter space.

$\mathcal{O}(1/R)$ singularity. Similarly, the surface integral arising from the \mathbf{K} -operator is also $\mathcal{O}(1/R)$. These surface integrals can be computed efficiently and to controllable accuracy using a Duffy transformation [17] and adaptive numerical quadrature. The contour integrals are non-singular and can be computed directly using one-dimensional adaptive quadrature routines.

The Duffy Transform

At this point it deems instructive to review the integration of a singular integral via the Duffy transformation. Consider the integration over a quadrilateral cell:

$$I(\vec{r}_m) = \vec{t} \cdot \int_S \bar{\bar{K}}(\vec{r}_m, \vec{r}') \cdot \vec{J}(\vec{r}') ds' = \vec{t} \cdot \int_{u^2=0}^1 \int_{u^1=0}^1 \bar{\bar{K}}(\vec{r}_m, \vec{r}'(u^1, u^2)) \cdot \vec{J}(\vec{r}'(u^1, u^2)) \sqrt{g} du^1 du^2 \quad (27)$$

where $\bar{\bar{K}}$ represents a dyadic kernel that has a $1/R$ singularity at \vec{r}_m and it is assumed that $\vec{r}_m \in S$. Initially, the quadrilateral cell is triangulated with a set of triangles that share a common point at \vec{r}_m , which is defined by local unitary coordinates (u_m^1, u_m^2) . This is depicted in the unitary space in Fig. 3 (a). The integration over the quadrilateral is then expressed as a superposition of the integration over each ‘‘Duffy triangle.’’ Each Duffy triangle is then mapped into a parametric space as illustrated in Fig. 3 (b) such that the singular point is mapped to the edge $u = 0$. Thus,

$$I(\vec{r}_m) = \sum_{\ell=1}^{N_\Delta} \vec{t} \cdot 2A_\ell \int_{\zeta=0}^1 \int_{\xi=0}^1 \bar{\bar{K}}(\vec{r}_m, \vec{r}'(u^1, u^2)) \cdot \vec{J}(\vec{r}'(u^1, u^2)) \sqrt{g(u^1, u^2)} \xi d\xi d\zeta \quad (28)$$

where N_Δ is the number of Duffy triangles, and A_ℓ is the area of the ℓ -th triangle (computed in the unitary space). From Fig. 3 (b):

$$2A_\ell = |(\bar{u}_1 - \bar{u}_m) \times (\bar{u}_2 - \bar{u}_m)|. \quad (29)$$

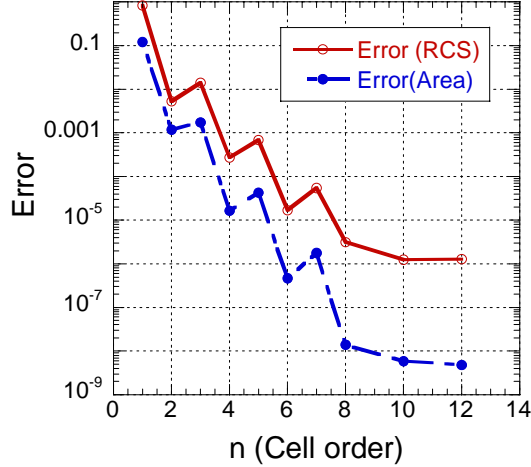


Fig. 4 Relative mean error in the RCS of a sphere of radius $k_o a = 6$ computed via the LCN method with ninth-order basis versus the interpolation order n of the 24 curvilinear cells. Also compared in the graph is the relative error of the area of the patched sphere.

There is also a simple linear mapping from the parametric coordinates to the unitary coordinates:

$$\vec{u} = (u^1, u^2) = (1 - \xi)\vec{u}_m + \xi(1 - \zeta)\vec{u}_1 + \xi\zeta\vec{u}_2. \quad (30)$$

When evaluating (28), one first computes (u^1, u^2) from the parametric coordinates and then computes $\vec{r}'(u^1, u^2)$, the unitary vectors and \sqrt{g} . Though, it is worth noting that since the current basis functions in (11) normalized by \sqrt{g} , this term cancels in an actual implementation.

VI. Some Numerical Results

We have implemented the LCN solution for a number of integral operators and have reported the results in [2, 4, 10, 12, 14]. Additional studies have been reported in [1, 5, 18]. Here we present a few examples mainly to study the convergence characteristics of the LCN method. Initially, we will study the electromagnetic scattering by a PEC sphere of radius a defined by $k_o a = 6$. The sphere was discretized with 24 quadrilateral curvilinear cells as defined in Section IV. Initially, the basis function order was set to $p = 9$. Similarly, a 9×9 -point Gauss-Legendre quadrature rule was used for the Nyström discretization of each patch. Thus, there are a total of 3,888 unknowns. Then, the order of the cells was increased from $n = 1$ to $n = 12$. The bistatic RCS was then computed for the sphere and the mean relative error was calculated relative to a Mie-series solution as:

$$\text{Mean Error} = \frac{1}{N_a} \sum_{i=1}^{N_a} \frac{|\sigma^{LCN}(\theta_i, \phi_i) - \sigma^{Mie}(\theta_i, \phi_i)|}{|\sigma^{Mie}(\theta_i, \phi_i)|} \quad (31)$$

where N_a is the number of angles (360 uniformly spaced angles were computed). A graph of the mean relative error versus the cell order n computed for the MFIE is illustrated in Fig. 4. The error in the area of the sphere as approximated via the 9×9 -point Gauss-Legendre quadrature rule is also graphed in Fig. 4 as a comparison. Initially, it is observed that error in the RCS and the area follow the same general trend. It also appears that the minimum error is reached when

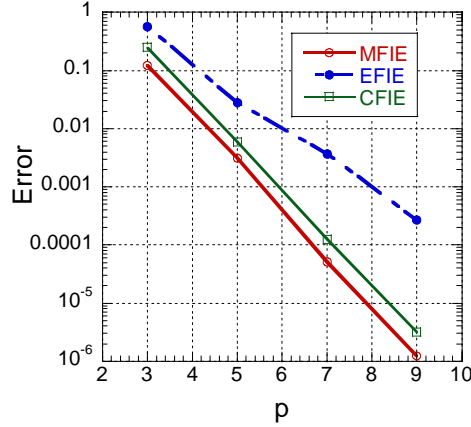


Fig. 5 Relative mean error in the RCS of a sphere of radius $k_0 a = 6$ computed via the LCN method versus the basis order p .

$n = p + 1$. It is also observed that even cell orders (which have an odd number of points) converge at a different rate than odd cell orders for an odd-order quadrature rule.

Next, the error in the RCS was computed for the sphere as a function of the basis order. In each case, the cell order is set so that $n = p + 1$. The RCS was predicted via the MFIE ($\alpha = 0$ in (10)), the EFIE ($\alpha = 1$) and the CFIE ($\alpha = 0.1$), and the mean error was predicted via (31). A graph of the mean relative error versus order p is illustrated in Fig. 5 for $p = 3, 5, 7$, and 9. The MFIE is converging optimally with the error decreasing nearly two orders of magnitude as p is increased by 2 orders. The EFIE is converging at a slower rate, and the CFIE is somewhat in-between. It is also noted that the number of degrees of freedom for each case is equal to $24 \times 2p^2$, since there are 24 cells, p^2 basis and quadrature points, and 2 vector projects per quadrature point. Finally, Fig. 6 illustrates the bistatic RCS for $p = 5$ as compared to the Mie-series solution. There is no observable difference for the MFIE and CFIE solutions, and only a very slight discernable difference for the EFIE solution. These simulations required only 1200 unknowns. We should also point out that the average patch edge length is $\sim 0.75 \lambda_0$. Thus, with $p = 5$, this corresponds to a discretization of < 7 unknowns per linear wavelength.

Finally, we illustrate the scattering by the EMCC metallic ogive [19]. The curvilinear cell discretization of the ogive is illustrated in Fig. 7 (288 cells $n = 7$). The ogive is 10 inches long along the major axis and has a 1 inch radius at the center. The monostatic RCS of the ogive at 9 GHz computed in the 0° elevation plane ($\theta = 90^\circ$) is illustrated in Fig. 8. This was computed via the MFIE with $p = 4$. These results compare extremely well to the measured data and predictions by Cicero in Fig. 9, pg. 86 of [19]. At this frequency, the ogive is approximate $7.6 \lambda_0$ long and has a radius of $0.76 \lambda_0$ at the center. These results were obtained using only 9,216 unknowns.

Acknowledgements

This work has been sponsored by the DARPA VET program through grant MDA971-01-1-0022 and the Army Research Office through contract DAAD-19-99-1-0093 with the University of Kentucky. The authors would also like to acknowledge the Computational Physics Group at HRL Laboratories, Malibu CA, for their pioneering work on the LCN method.

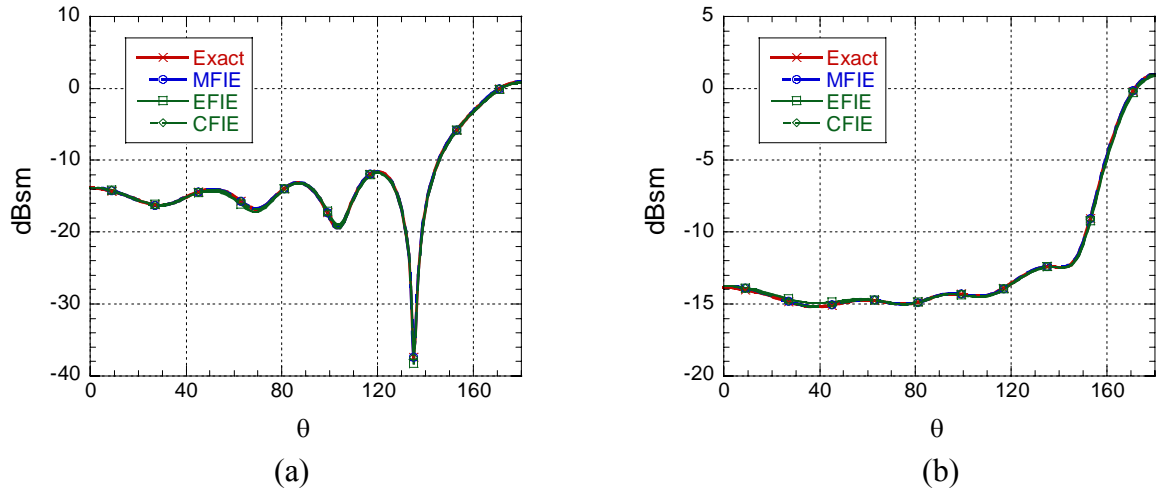


Fig. 6 Bistatic RCS of a sphere of radius $k_o a = 6$ computed via the LCN solution of the MFIE, EFIE, and CFIE compared to an exact Mie series solution (24 cells, $p = 5$, $n = 6$).

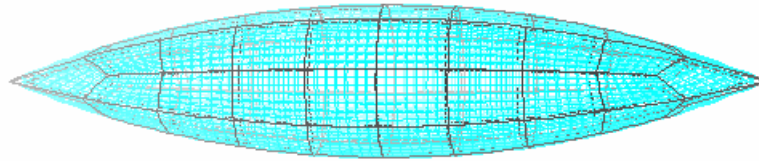


Fig. 7 The EMCC metallic ogive [19] approximated by 72 curvilinear cells ($n = 7$).

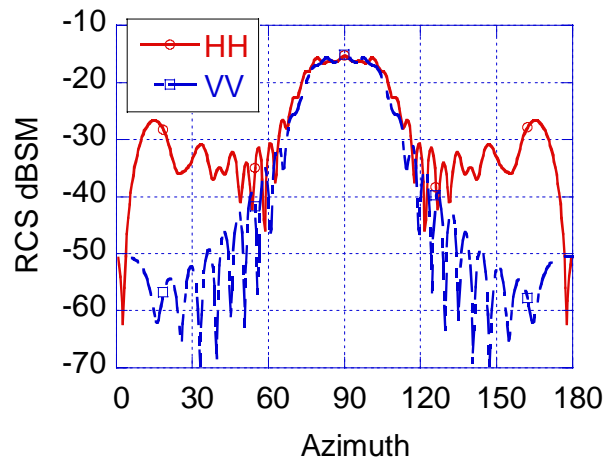
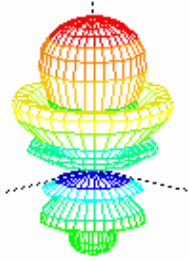


Fig. 6 Monostatic RCS of the EMCC metallic ogive at 9 GHz.

References

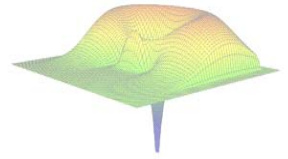
- [1] L. F. Canino, J. J. Ottusch, M. A. Stalzer, J. L. Visher, and S. M. Wandzura, "Numerical solution of the Helmholtz equation in 2D and 3D using a high-order Nyström discretization," *Journal of Computational Physics*, vol. 146, pp. 627-663, 1998.
- [2] S. D. Gedney, "On Deriving a Locally Corrected Nyström Scheme from a Quadrature Sampled Moment Method," *IEEE Transactions on Antennas and Propagation*, vol. 51, pp. 2402-2412, 2003.
- [3] G. Liu and S. D. Gedney, "High-Order Moment Method Solution for the Scattering Analysis of Penetrable Bodies," *Electromagnetics*, vol. 23, 2003.
- [4] S. D. Gedney and C. C. Lu, "High-Order Solution for the Electromagnetic Scattering by Inhomogeneous Dielectric Bodies," *Radio Science*, vol. 38, pp. 1015, 2003.
- [5] A. F. Peterson, "Accuracy of currents produced by the Locally-corrected Nyström method and the Method of Moments when used with higher-order representations," *Applied Computational Electromagnetics Society Journal*, vol. 17, pp. 74-83, 2002.
- [6] C. Müller, *Foundations of the Mathematical Theory of Electromagnetic Waves*, vol. 301. Berlin: Springer-Verlag, 1969.
- [7] R. F. Harrington, "Boundary integral formulations for homogeneous material bodies," *Journal of Electromagnetic Waves and Applications*, vol. 3, pp. 1-15, 1989.
- [8] X. Q. Sheng, J. M. Jin, J. M. Song, W. C. Chew, and C. C. Lu, "Solution of combined-field integral equation using multilevel fast multipole algorithm for scattering by homogeneous bodies," *IEEE Transactions on Antennas and Propagation*, vol. 46, pp. 1718-1726, 1998.
- [9] A. F. Peterson, S. L. Ray, and R. Mittra, *Computational Methods for Electromagnetics*. New York: IEEE Press, 1998.
- [10] S. D. Gedney, "High-Order Method of Moment Solution of the Scattering by Three-Dimensional PEC Bodies using Quadrature Based Point Matching," *Microwave and Optical Technology Letters*, vol. 29, pp. 303-309, 2001.
- [11] J. A. Stratton, *Electromagnetic Theory*. New York: McGraw-Hill, 1941.
- [12] S. D. Gedney, "Application of the High-Order Nyström Scheme to the Integral Equation Solution of Electromagnetic Interaction Problems," presented at IEEE International Symposium on Electromagnetic Compatibility, Washington, D.C., 2000.
- [13] F. Çaliskan and A. F. Peterson, "The need for mixed-order representations with the locally corrected Nystrom method," *IEEE Antennas and Wireless Propagation Letters*, vol. 2, pp. 72- 73, 2003.
- [14] S. D. Gedney, A. Zhu, and C. C. Lu, "Study of mixed-order basis functions for the locally-corrected Nyström method," *IEEE Transactions on Antennas and Propagation*, submitted, 2003.
- [15] A. H. Stroud, *Approximate Calculation of Multiple Integrals*. Englewood Cliffs, NJ: Prentice-Hall, 1971.
- [16] P. P. Silvester and R. L. Ferrari, *Finite Elements for Electrical Engineerings*, 2nd ed. Cambridge: Cambridge University Press, 1990.
- [17] M. G. Duffy, "Quadrature over a pyramid or cube of integrands with a singularity at a vertex," *SIAM Journal on Numerical Analysis*, vol. 19, pp. 1260-1262, 1982.

- [18] K. C. Donepudi, J. M. Jin, S. Velamparambil, J. M. Song, and W. C. Chew, "A higher order parallelized multilevel fast multipole algorithm for 3-D scattering," *IEEE Transactions on Antennas and Propagation*, vol. 49, pp. 1069-1078, 2001.
- [19] A. C. Woo, H. T. G. Wang, and M. J. Schuh, "Benchmark radar targets for the validation of computational electromagnetics programs," *IEEE Antennas and Propagation Magazine*, vol. 35, pp. 84-89, 1993.



ACES

Applied Computational Electromagnetic Society



ACES Web Site: <http://aces.ee.olemiss.edu>

CALL FOR PAPERS

**The 20th Annual Review of Progress in Applied Computational
Electromagnetics, April 19-23, 2004**
Sheraton Syracuse University Hotel and Conference Center
Syracuse, New York

The 20th Annual Review of Progress in Applied Computational Electromagnetics Symposium will be held for the first time outside Monterey. The location is the Sheraton Syracuse University Hotel and Conference Center in Syracuse, New York, which will accommodate all the technical sessions on the same floor and the lodgings for all the attendees. It is an ideal opportunity to participate in a large gathering of EM analysis enthusiasts. The purpose of the Symposium is to bring developers, analysts, and users together to share information and experience about the practical application of EM analysis using computational methods. The symposium offers technical presentations of all aspects of electromagnetic computational analysis and applications.

Papers may address general issues in applied computational electromagnetics or may focus on specific applications, techniques, codes, or computational issues of potential interest to the applied computational electromagnetics community. All authors of accepted papers will have the option to submit an extended version of their paper or papers for review and publication in special issues of the ACES Journal. Suggested session topics follow, although contributions in other areas of computational electromagnetics are encouraged and will be considered.

Proposed Topics:

Low frequency electromagnetic applications	Time domain methods
Asymptotic and high frequency techniques	Hybrid techniques
Finite element methods	Inverse scattering techniques
Fast and efficient CEM methods	Wave propagation
Wavelet and TLM modeling	MEMS and MMIC
Computational bio-electromagnetics	EMC/EMI
Radar and remote sensing applications	Smart antennas and arrays
Neural network techniques for CEM	Mobile and PCS antennas
Optimization techniques for CEM	RF and microwave devices
Integral or Differential Equations	Phased array antennas
Wideband and multi-frequency antennas	Signal processing antennas

SYMPOSIUM STRUCTURE

The annual ACES Symposium includes: oral-invited sessions, poster sessions, a student paper competition, short courses (*full-day* and *half-day*), an awards banquet, vendor exhibits, and social events. The ACES Symposium will include panel sessions, where invited speakers deliver original essay-like reviews of topics of current interest to the computational electromagnetics community.

PAPER FORMATTING REQUIREMENTS

The recommended paper length, including text, figures, tables and references, is four (4) pages, with eight (8) pages as a maximum. Submitted papers should be formatted for 8.5x11-inch U.S. standard paper, with 1-inch top, bottom and side margins. On the first page, the title should be 1-1/2 inches from top with authors, affiliations, and e-mail addresses beneath the title. **Use single line spacing, with 11- or 12-point size of Times New Roman or Times font. Please do not use Asian fonts. No typed page numbers, headers or footers.** The entire text should be fully justified (flush left and flush right). A model paper can be found in the conference section on ACES web site at: <http://aces.ee.olemiss.edu>. Each paper should be submitted in camera-ready format with good resolution and clearly readable.

PAPER SUBMISSION PROCEDURE

No email, fax or hard-copy paper submission will be accepted. Papers are required, in Adobe Acrobat (version 5 or later) or in Microsoft Word 2000 format and must be submitted through ACES web site using the “Paper Submission” button in the left menu, followed by the selection of the “Conference” option, and then following the on-line submission instructions. Successful submission will be acknowledged automatically by email after completing all uploading procedure as specified on ACES web site.

SUBMISSION DEADLINE AND REGISTRATION REQUIREMENT

Submission deadline is **November 1, 2003**. A signed ACES copyright-transfer form must be mailed to the conference chair immediately following the submission as instructed in the acknowledgment of submission email message. Papers without an executed copyright form will not be considered for review and possible presentation at the conference. Upon the completion of the review process, by the technical program committee, the acceptance notification along with the pre-registration information will be mailed to the corresponding author on or about **December 10, 2003**. Each presenting author is required to complete the paid pre-registration and the execution of any required paper corrections by **February 1, 2004** for final acceptance for presentation and inclusion in the symposium proceedings.

BEST-PAPER PRIZE

A **\$500** prize will be awarded to the authors of the best non-student paper presented (poster or oral) at the 20th Annual Review. Papers will be judged by the ACES prize-paper committee.

BEST STUDENT PAPERS CONTEST

The best three (3) student papers presented at the 20th Annual Review will be announced at the symposium banquet. Student papers submitted for this competition will be judged by three (3) members of the ACES Board of Directors. The first, second, and third winners will be awarded cash prizes of **\$300, \$200, and \$100**, respectively.

For any additional information, including travel and lodging, please contact the conference Chair: **Tapan K. Sarkar** (tk Sarkar@svr.edu, Tel: 315-443-3775, Fax: 315-443-4441), or visit ACES web site at: <http://aces.ee.olemiss.edu>.

Symposium Chair	Symposium Co-Chair	Symposium Administrator	Short Course Chair	Exhibits Chair	Publicity Chair
<i>Tapan K. Sarkar</i>	<i>Atef Elsherbeni</i>	<i>Richard W. Adler</i>	<i>John Shaeffer</i>	<i>Andrew L. Drozd</i>	<i>Omar M. Ramahi</i>
Syracuse University	The University of Mississippi	Naval Postgraduate School	Retired CEM Enthusiast	ANDRO Consulting	University of Maryland

APPLIED COMPUTATIONAL ELECTROMAGNETICS SOCIETY
RICHARD W. ADLER, EXECUTIVE OFFICER
ECE DEPARTMENT, CODE ECAB, 833 DYER ROAD, ROOM 437
NAVAL POSTGRADUATE SCHOOL, MONTEREY, CA 93943-5121,
PHONE: 831-646-1111 FAX: 831-649-0300
EMAIL: RWA@ATTGLOBAL.NET

Please print

LAST NAME	FIRST NAME	MIDDLE INITIAL
COMPANY/ORGANIZATION/UNIVERSITY	DEPARTMENT / MAIL STATION	
MAILING ADDRESS WHERE PUBS MAY BE MAILED		
CITY	PROVINCE/STATE	COUNTRY
		ZIP/POSTAL CODE
TELEPHONE	FAX	AMATEUR RADIO CALL SIGN
		E-MAIL ADDRESS

	NEW MEMBERSHIP RATES (EFFECTIVE JANUARY 2003)			
	BASIC	INTERMEDIATE	EXPANDED	INSTITUTIONAL
WORLD AREA	Journal & Newsletter Access via Website & Annual (Nov) Searchable CD Rom of Proceedings of March Conference & Searchable CD ROM of year's Journals	BASIC, plus CD ROM of March Journal (Mar) & CD ROM of July Journal (Jul)	BASIC, plus Unbound Paper Copies of Journals (Mar, Jul, Nov)	BASIC, plus Bound Paper Copies of Journals (Mar, Jul, Nov)
US, CANADA and MEXICO	\$35. USD	\$55. USD	\$90. USD	\$125. USD
ALL OTHER AREAS	\$35. USD	\$55. USD	\$110. USD	\$125. USD

FULL-TIME STUDENT/RETIRED/UNEMPLOYED: BASIC RATE IS \$20.00 USD FOR ALL COUNTRIES

Non-USA participants: Prices are in U.S. dollars. All currencies must be converted to U.S. dollars payable by banks with U.S. affiliates. (1) Bank Checks must have U.S. address of bank; Checks are payable to "ACES", (2) U.S./International Money Order drawn in U.S. funds, payable in U.S. \$\$, (3) Credit Cards: Visa, MasterCard, Amex and Discover.

CREDIT CARD USERS

PRINT CARD HOLDER NAME: _____

CREDIT CARD HOLDER SIGNATURE: _____

CREDIT CARD HOLDER ADDRESS: _____

ADDRESS, CONT: _____

CREDIT CARD ACCOUNT #: _____

CARD EXP. DATE: _____

ADVERTISING RATES		
	FEE	PRINTED SIZE
Full page	\$200	7.5" × 10.0"
1/2 page	\$100	7.5" × 4.7" or 3.5" × 10.0"
1/4 page	\$50	3.5" × 4.7"
<p>All ads must be camera ready copy.</p> <p>Ad deadlines are same as Newsletter copy deadlines.</p> <p>Place ads with Ray Perez, Newsletter Editor, Martin Marietta Astronautics, MS 58700, PO Box 179, Denver, CO 80201, USA. The editor reserves the right to reject ads.</p>		

DEADLINE FOR THE SUBMISSION OF ARTICLES	
Issue	Copy Deadline
March	February 1
July	June 1
November	October 1

For the **ACES NEWSLETTER**, send copy to Bruce Archambeault in the following formats:

1. A PDF copy.
2. A MS Word (ver. 97 or higher) copy. If any software other than WORD has been used, contact the Managing Editor, Richard W. Adler **before** submitting a diskette, CD-R or electronic file.

Last Word

The most incomprehensible thing about the world is that it is at all comprehensible.

----Albert Einstein